

# Structured MIMO $\mathcal{H}_\infty$ Design for Dual-Stage Inertial Stabilization: Case Study for HIFOO<sup>☆</sup>

Martin Řezáč and Zdeněk Hurák

Faculty of Electrical Engineering, Czech Technical University in Prague, Czech Republic  
(e-mail: rezac.martin@fel.cvut.cz and hurak@fel.cvut.cz).

## Abstract

The paper reports on a control design for an experimental platform that contains two aligned motorized gimbals stabilizing an optical payload around a single axis using measurements from an inertial angular rate sensor (MEMS gyro). Such a laboratory system represents a simplified testbed for the more practically useful line-of-sight inertial stabilization system. The paper defends the choice of the control configuration and argues that when using MIMO design procedures, enforcing some structure upon the transfer function matrix makes the controller implementation and fine-tuning easier. Such structural constraints were taken into consideration in the computational  $\mathcal{H}_\infty$  design by using the publicly available HIFOO solver based on algorithms for non-convex and non-smooth optimization. As an extra feature, the resulting controller is also of low order, namely the (sub)controllers are of PI type. Results are contrasted with the controllers designed with classical methods and full MIMO  $\mathcal{H}_\infty$  optimization. Both simulations and laboratory experiments were used to validate these findings.

**Keywords:** Inertial stabilization, H-infinity control, robust control, structural constraints, dual-stage.

## 1. Introduction

This paper documents a computational design of a feedback controller for an electromechanical system (Fig. 1 right) that uses two aligned motorized gimbals (joints, shafts) to rotate an optoelectronic payload such as cameras and/or laser range-finders and/or markers around a single (!) axis. Besides orienting the payload upon command, the other key role of the control system is to isolate the inertial orientation of the payload from an unwanted disturbing rotational motion of the platform base, thus emulating the realistic scenario when the platform is carried on some mobile vehicle (car, ship, unmanned aircraft).

In order to turn the introduced experimental platform into a practically useful system, at least one more rotational degree of freedom (around a different rotational axis) would have to be added so that inertial stabilization of the optical axis of a payload is feasible, resulting in the so-called inertial line-of-sight stabilization surveyed by Hilkert (2008) and Masten (2008). A platform of this type with four degrees of rotational freedom is indeed being built by the authors (Fig. 1 left). Nonetheless, the objective of this paper is to explore in some depth the single-axis case first because the added complexity due to two controlled gimbals rotating around a common axis makes the problem nontrivial. Hurák and Řezáč (2009) and Hurák and Řezáč (In Press) have already presented some control design issues related to a more conventional double-gimbal inertially stabilized

camera platform where rotation about each axis is induced by a single DC direct drive motor. The present work constitutes a step towards an upgrade of that technology where the popular double gimbal system is replaced by a quadruple of gimbals. This mechanical configuration can be viewed as giving dual driving for both axis of rotation. Hence the concept of *dual-stage control* is invoked.

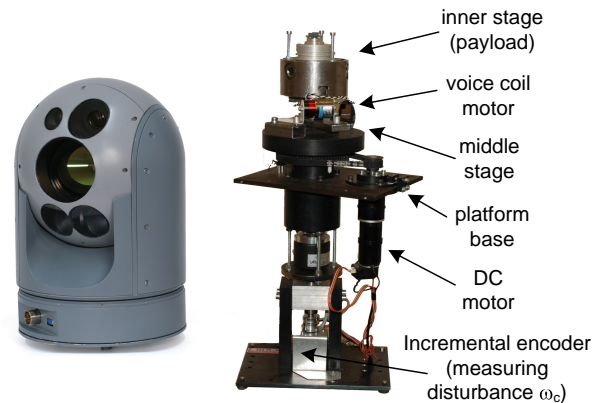


Figure 1: Left: The prototype of inertially stabilized platform with dual-stage mechanism. Platform was developed by Czech Air Force and Air Defence Technological Institute (Vojenský ústav letectva a PVO) in collaboration with Czech Technical University in Prague and ESSA company. Right: Experimental system for benchmarking dual-stage inertial stabilization algorithms. The inner gimbal is actuated by a linear voice coil motor, which imposed stringent limits on the angular range ( $\pm 5^\circ$ ).

<sup>☆</sup>This work was supported by the Ministry of Education of the Czech Republic within the project called Center for Applied Cybernetics (1M0567) and by Ministry of Industry and Trade of the Czech Republic within TIP FR-TI1/265.

### 1.1. Survey of related literature

Related research can be found under the label of *dual-stage control* in the area of positioning of read/write (R/W) heads in some modern hard disk drives. It is reported, for instance, by Herrmann and Guo (2004); Horowitz et al. (2007); Suthasun et al. (2004) and Schroeck et al. (2001). In order to see how much inspiration can be taken from this area, let us describe the basic principle. A rotating arm with an R/W head at one end is actuated by a rotary voice-coil motor at the other end, which can bring the R/W head onto the required position (track). Standard hard disks live with just this configuration. The upgrade consists in fabrication of the tip of the arm such that a tiny flexible joint with a very limited angle is created there. Deflection of the very tip with the R/W head is then actuated by contracting/extracting piezoelectric microactuators. This creates the second stage with fine and fast pointing. Another application of the same principle but applied rather in positioning of the tip-tilt table than to HDD head is reported by Woody and Smith (2006) and in rotational table by Zheng et al. (2011).

Obviously, the difference between the concepts of dual-stage control in hard-disk drives and inertial platforms is that in the former the contribution of two actuators is *added* (voice-coil motor responsible for large angular deflection and piezos for a tiny but fast refinement) whereas in the latter the inner gimbal is (theoretically) *decoupled* from the motion of the outer gimbal. This decoupling is the key property in inertially stabilized systems since the Newton second law works for us through so-called *mass stabilization*.

To the best of the authors' knowledge, use dual-stage concept in the area of inertial line-of-sight stabilization is not documented in the literature. Perhaps the only exception is Lyou et al. (2009), who focus more on the image processing related issues rather than inertial sensing based stabilization.

There is yet another application area where the issue of controlling a single variable using two actuators has been studied in a context almost identical to the one presented here. It is denoted *mid-range control* and is explained in some process control texts, for instance, by Åström and Hägglund (2005).

### 1.2. $\mathcal{H}_\infty$ design with structural constraints

In this paper, the already classical  $\mathcal{H}_\infty$  control design methodology is followed. It will be shown, however, that the particular control problem presented in this paper naturally invokes a requirement on a structure of the MIMO controller. By the term *structure* we mean that some of the transfer functions are fixed to zero. Such design constraints are tremendously difficult to take into account in an optimization-based control design because they render the set of admissible controllers non-convex. One of the contributions of this paper, apart from the discussion of the control configuration as such, is a well-documented practical application of one concrete numerical solver for fixed structure and fixed order  $\mathcal{H}_\infty$  control design. Namely, the HIFOO solver for Matlab recently released into a public domain by Gumussoy et al. (2009) was used. This paper can be partially viewed as a case study for such a powerful and useful tool.

## 2. Experimental setup for single-axis dual-stage inertial stabilization

In order to investigate the control issues arising in inertially stabilized platforms with dual joints, a single-axis dual-stage benchmark platform has been designed and built (see the photo in Fig. 1, detail in Fig. 2 and the sketch in Fig. 3). It consists of two electrical motors rotating the payload around a single (vertical) axis. The outer motor is the brushed rotary DC motor RE36 produced by Maxon (type 118800 with a planetary gear-head GP42C type 203123). It carries the inner stage motorized by a linear voice-coil motor type NCC05-11-011-1X by H2W Technologies, which in turn actuates the dummy payload (in a real application this would be a camera, laser marker or range finder etc.). The inertial angular speed of the payload is measured by MEMS gyro ADIS 16255 by Analog Devices.

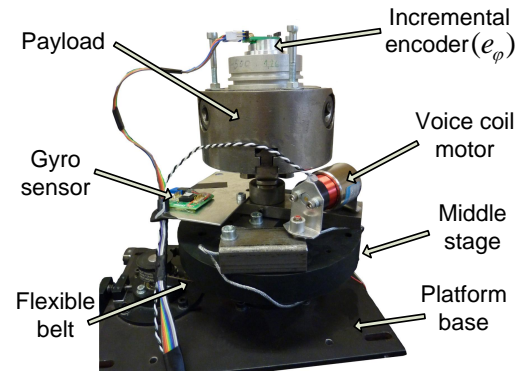


Figure 2: The detail of the upper dual-stage part of the benchmarking system.

### 2.1. Notation and coordinate frames

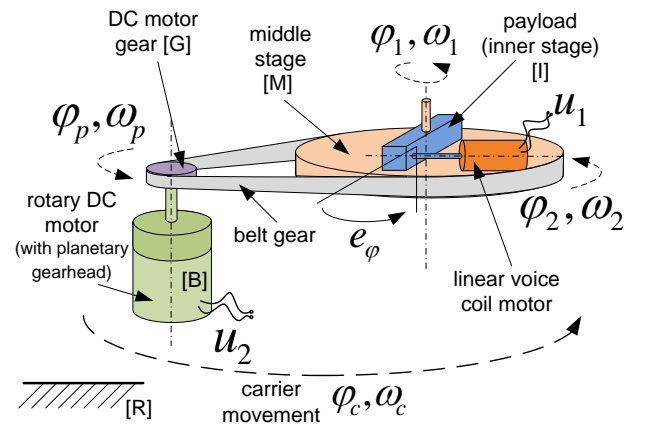


Figure 3: Mechanical scheme of dual-stage system. Angles and rates denoted by dashed arrows stand for inertial quantities (with respect to reference frame [R]).

Building a mathematical model, several coordinate frames are needed as seen in Fig. 3. These are: the reference frame [R] attached to the ground, the platform base frame [B] (green), the

middle stage frame [M] (orange) and the inner stage frame [I] (blue). The frames [M] and [B] are connected via the DC rotary motor and a (flexible) belt gear. The frame [G] is attached to the output shaft of the DC motor. The frames [M] and [I] are then connected through the linear voice coil motor, which exerts a torque. The inertial angular rate of the shaft of the DC motor is denoted  $\omega_p$ , the inertial angular rate of the middle stage, which is dynamically connected to the DC motor via a belt gear and which hosts the "stator" of the voice coil motor, is denoted  $\omega_2$ . The inertial angular rate of the payload as measured by the attached MEMS gyro and actuated by the VCM is denoted  $\omega_1$ . The remaining variables are the inertial angular rate of the carrier denoted  $\omega_c$ , which in this particular application is measured through a measurement of the angle  $\varphi_c$  using an incremental encoder. Another angular measurement is the misalignment  $e_\varphi$  between the inner stage and the middle stage. Whereas the rotary DC motor can rotate  $n$  times  $360^\circ$ , the inner stage misalignment angle  $e_\varphi$  is limited to  $\pm 5^\circ \approx \pm 0.087$  rad.

### 3. Feedback control configuration

The key task for the control system is to bring the inertial angular rate  $\omega_1$  of the payload to a desired value and keep it there irrespectively of the disturbing rotational motion of the carrier given by the rate  $\omega_c$ . When there is no request to redirect the payload, the task is to keep the payload still, that is,  $\omega_1^{ref} = 0$ , while keeping the angular misalignment  $e_\varphi$  between the inner and the outer gimbals in the middle of the range, that is  $e_\varphi = 0$  so as not to hit the mechanical limits.

Now, which motor is responsible for what? As a matter of fact, both motors can participate in both tasks leading to a full MIMO controller, but from the viewpoint of simplicity of implementation and fine-tuning, a decision was made to assign "roles" to the motors. Regulation of the angular rate  $\omega_1$  or tracking of its reference value  $\omega_1^{ref}$  is achieved by applying the voltage  $u_1$  produced by the controller  $K_1$  and applied to the VCM. This is the *inertial angular velocity control loop*. The *angular deviation loop* measures the angle  $e_\varphi$  and pushes this value to zero by applying the voltage  $u_2$  computed by the controller  $R_2$  to the windings of the rotary DC motor. Block diagram is in Fig. 4.

Furthermore, a major improvement in regulating the angle  $e_\varphi$  can be achieved by introducing a feedforward term  $F$  from the reference rate  $\omega_1^{ref}$  to the voltage  $u_2$ . The presence of this term can be easily justified. A classical feedforward controller in motion control applications takes the reference angle  $\varphi_1$ , differentiates it twice in order to obtain a variable equivalent to a torque and then scales it and adds to the system input  $u_2$ . But here the value of  $\varphi_1$  is not measured. Instead, the dynamics from  $\omega_1^{ref}$  to  $\varphi_1$  is known (determined by the already designed controller  $K_1$ ). The purpose of the feedforward controller is to the shape signal  $\omega_1$  and apply it to the outer stage (DC motor) so that the misalignment angle  $e_\varphi$  is kept small (or possibly zero). In other words, when there is a nonzero inertial rate to be tracked by the payload, it is not only the VCM motor that starts working but also the rotary DC motor that receives an

immediate command. It does not wait for the error  $e_\varphi$  to build up.

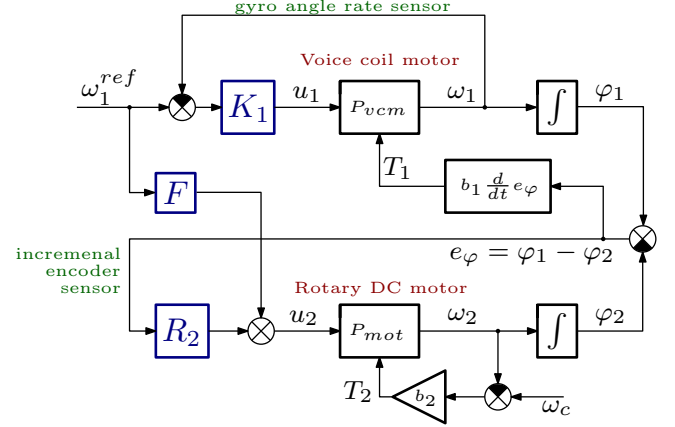


Figure 4: Feedback control configuration. It is only for the sake of simplicity of the figure that the reaction torque generated by the VCM and applied to the rotary motor is not depicted here and neither are the back emf voltages, which are derived from the relative and not the inertial rates.

### 4. Model of dynamics

This section develops a model of dynamics of the system. The list of all components and their parameter values is in Table 1.

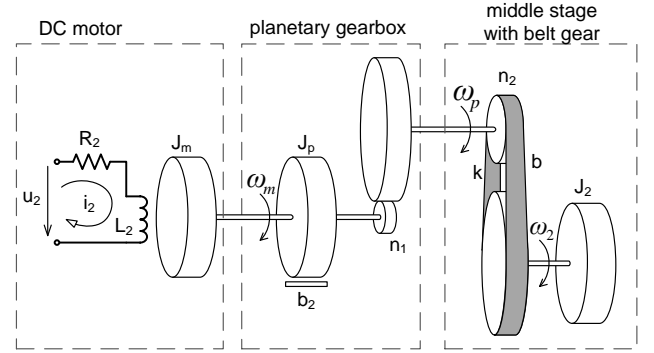


Figure 5: DC motor with a planetary gearbox and a belt gear.

The structure of the DC motor with a gearbox and an external flexible belt gear is depicted in Fig. 5. The structure is modeled as a classical DC motor with an electrical and mechanical parts and with a viscous friction  $b_p$  in the bearings. The belt gear is modeled as a double-mass-spring system with the spring constant  $k$  and damping  $b$ . Most of the parameters listed in Table 1 are known from the motor's datasheet, the remaining ones –  $k$ ,  $b$ ,  $b_p$  and  $J_2$  – were identified using gray-box model fitting methods available in System Identification Toolbox for Matlab. The model is represented by (3) through (7).

The voice coil motor, described by (1) and (2), is modeled as a classical DC motor as well. But it is a linear motor, thus

Table 1: Technical parameters of the components.

Par.	Description	Value	Units
$x_s$	VCM stroke length	12.7	mm
$F_c$	VCM continuous force	4.9	N
$F_p$	VCM peak force	14.7	N
$k_m$	VCM motor constant	2.95	N/√W
$R_1$	VCM resistance	2.9	Ω
$L_1$	VCM inductance	0.99	mH
$k_{t1}$	VCM force constant	5.11	N/A
$k_{e1}$	VCM back emf constant	5.11	V/(m/s)
$m_{t1}$	VCM total mass	144	g
$m_{m1}$	VCM moving part mass	27	g
$b_1$	VCM viscous friction	0.125	Nms/rad
$U_{1max}$	VCM supply voltage	7	V
$r$	radius of action of VCM	65	mm
$J_1$	payload moment of inertia	10	gm <sup>2</sup>
$k_{t2}$	rot. motor torque constant	56.6	mNm/A
$k_{e2}$	rot. motor back emf	169	rpm/V
$R_2$	rot. motor resistance	2.74	Ω
$L_2$	rot. motor inductance	0.487	mH
$U_{2max}$	rot. motor supply voltage	32	V
$J_m$	rot. motor mmnt. of inertia	67.8	gcm <sup>2</sup>
$b_p$	rot.m. viscous friction	0.48	Nm/(rad/s)
$n_1$	planetary gear-head ratio	74:1	-
$J_p$	planetary gear-head inertia	15	gcm <sup>2</sup>
$T_m$	max torque at gear output	15	Nm
$b_m$	avg. backlash at gear output	0.5	°
$J_2$	mid. stage mmnt. of inertia	25	gm <sup>2</sup>
$n_2$	belt gear ratio	4:1	-
$k$	spring constant for the belt	250	Nm/rad
$b$	damping of the belt	0.9	Nm/(rad/s)
$f_{bw}$	ADIS 16255 analog bandwidth	50	Hz
$\omega_{max}$	ADIS 16255 maximum angular rate	5.59	rad/s

the applied force needs to be transformed into a torque. The projection of the force into a torque depends nonlinearly on the angle  $e_\varphi$ . Nonetheless, this effect is negligible for the prescribed bounds on the misalignment  $e_\varphi$ .

On the other hand, the friction in the inner stage bearings cannot be neglected since it is significant enough to disturb the inertial rate of the payload when the outer gimbal moves. As the first step, a linear (viscous) model represented by the constant  $b_1$  was used. Of course, in order to obtain more realistic model that predicts the annoying stick-slip behavior at slow speeds, more advanced models should be used, for example the popular LuGre model proposed by Canudas de Wit et al. (1995) or by Ray et al. (2001). One way or another, the presence of friction causes undesired coupling between the payload and the carrier. Hence the transfer function from the disturbance  $\omega_c$  to  $\omega_1$  measured at the payload is certainly nowhere close to zero as one might desire. At very low frequencies it is even exactly equal to 1 (see the Fig. 6).

Equations (1) through (10) constitute the full state-space model of the dual-stage benchmark system. The state variables are chosen according to Fig. 4,  $i_1$  and  $i_2$  are the motor currents in [A], the inputs are the normalized voltages  $u_1$  and  $u_2$ .

State equations:

$$U_{1max} u_1 = R_1 i_1 + L_1 \frac{di_1}{dt} + r k_{e1} (\omega_1 - \omega_2), \quad (1)$$

$$J_1 \dot{\omega}_1 = r k_{t1} i_1 - b_1 (\omega_1 - \omega_2), \quad (2)$$

$$U_{2max} u_2 = R_2 i_2 + L_2 \frac{di_2}{dt} + n_1 k_{e2} (\omega_p - n_2 \omega_c), \quad (3)$$

$$n_1^2 (J_m + J_p) \dot{\omega}_p = n_1 k_{t2} i_2 - k (\varphi_p - n_2 \varphi_2) - b (\omega_p - n_2 \omega_2) - b_p (\omega_p - n_2 \omega_c), \quad (4)$$

$$J_2 \dot{\omega}_2 = k (\varphi_p - n_2 \varphi_2) + b (\omega_p - n_2 \omega_2) - r k_{t1} i_1, \quad (5)$$

$$\dot{\varphi}_p = \omega_p, \quad (6)$$

$$\dot{\varphi}_2 = \omega_2, \quad (7)$$

$$\dot{\varphi}_1 = \omega_1. \quad (8)$$

Output equations:

$$y_1 = \omega_1, \quad (9)$$

$$y_2 = \varphi_1 - \varphi_2 = e_\varphi. \quad (10)$$

The equations (1) through (10) may be written in terms of the system transfer function matrix  $G$

$$\begin{bmatrix} \hat{\omega}_1 \\ \hat{e}_\varphi \end{bmatrix} = G \begin{bmatrix} \hat{u}_1 \\ \hat{u}_2 \end{bmatrix}. \quad (11)$$

Fig. 6 shows the open-loop frequency responses of the two loaded motors independently. The magnitude response of the stage with the rotary DC motor is represented by two plots, one for the situation when angle  $e_\varphi$  is below the physical limits, and the other for the situation when it hits the mechanical limits and the rotary DC motor is then pulling the payload along. No bouncing back was modeled. The moment of inertia  $J_2$  of the outer stage then has to be increased by the moment of inertia of the payload  $J_1$ , hence the bandwidth is lowered.

## 5. Design of a structured MIMO low-order controller using HIFOO

HIFOO is a third-party Matlab toolbox developed by Gumusoy et al. (2009). The acronym stands for *H-infinity fixed-order optimization*. It relies on advanced techniques for non-convex non-smooth optimization and therefore it can design a fixed-order controller with a prespecified structure of the state space matrices. The former feature is universally welcome, the latter is appreciated in this particular project. The toolbox has been made freely available.

It is notoriously known that the design of an  $H_\infty$ -optimal controller can be written as the minimization

$$\min_K \|F_l(P, K)\|_\infty, \quad (12)$$

where  $F_l$  is lower fractional transformation,  $K$  is the searched controller and  $P$  is the augmented plant composed of both the original plant dynamics and the artificial weighting filters used

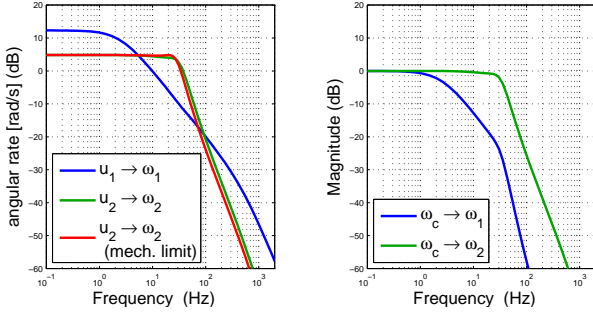


Figure 6: Left: Open-loop magnitude Bode plots for both stages. The inputs are the normalized voltages to the two motors, the output is the inertial angular rate [rad/s]. The output stage with the rotary DC motor is represented by two plots, one for the angular misalignment  $e_\varphi$  between the two stage within the mechanical limits and the other for the inner stage hitting the limits (= mech. limit), thus being pulled by the the outer one.

Right: Magnitude Bode plot for the disturbance attenuation (still open-loop). The inertial rate  $\omega_1$  is only affected by disturbance rate  $\omega_c$  at very low frequencies. The middle and high frequency ranges exhibit nice attenuation. In contrast, the inertial rate  $\omega_2$  is affected by  $\omega_c$  up to 40 Hz, higher frequency range is attenuated as well due to the elasticity of the belt gear.

to express the control objectives. A wealth of various software packages exist for solving this optimization problem. HIFOO stands out by being able to fix the order and the structure of the controller.

### 5.1. Augmented plant structure

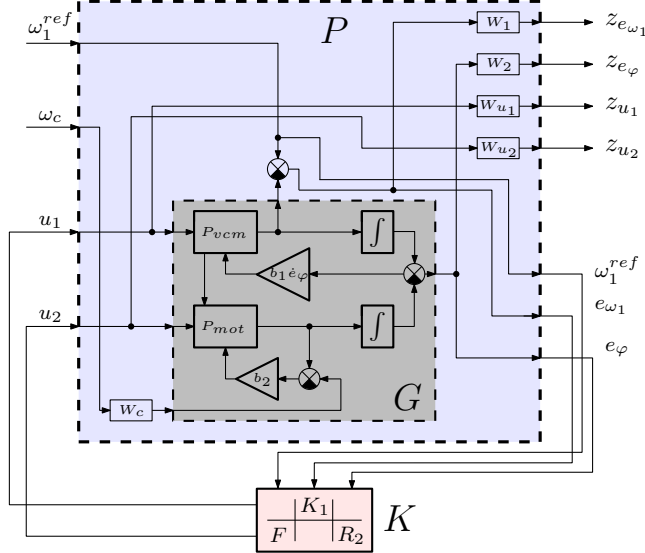


Figure 7: LFT of a augmented system and a structured controller. Sub-blocks of the controller  $K$  correspond to the feedback configuration as discussed in the section 3.

The augmented plant model is evident from Fig. 7. There are two exogenous variables:  $\omega_1^{ref}$ , and  $\omega_c$  and four regulated variables:  $z_{e\omega_1}$ ,  $z_{e\varphi}$ ,  $z_{u1}$  and  $z_{u2}$ , which are to be minimized by the feedback controller  $K$  (in the 2-norm). The variable  $z_{e\omega_1}$  specifies the weighted error between the required reference rate  $\omega_1^{ref}$  and the measured rate  $\omega_1$  from the gyro. Similarly, the variable

$z_{e\varphi}$  penalizes the deviation of  $e_\varphi$  from zero. The variables  $z_{u1}$  and  $z_{u2}$  put some weight on the actuator effort.

The controller  $K$  accepts the measurements from both sensors (the MEMS gyro giving the inertial angular rate  $\omega_1$  and incremental encoder giving the angle  $e_\varphi$ ) and the inertial reference rate  $\omega_1^{ref}$ . It produces two voltages  $u_1$  and  $u_2$ . It should be emphasized that this is just a reformulation of the configuration described in the section 3. That is, the controllers  $K_1$ ,  $R_2$  and  $F$  form the components  $K_{(1,2)}$ ,  $K_{(2,3)}$  and  $K_{(2,1)}$ , respectively, with the remaining sub-blocks of the compound controller  $K$  set to zero. Capability of handling such structural constraints was exactly the reason for adoption of HIFOO here.

One possibility to specify the state space structure of a compound controller  $K$  with zero terms  $K_{(1,1)}$ ,  $K_{(2,2)}$  and  $K_{(1,3)}$  of the controller transfer function matrix is to consider the controllers  $K_1$ ,  $R_2$  and  $F$  connected in parallel. The resulting state space model is characterized by the matrices  $A$ ,  $B$ ,  $C$ ,  $D$

$$A = \begin{bmatrix} A_{n_1 \times n_1} & 0 & 0 \\ 0 & A_{n_2 \times n_2} & 0 \\ 0 & 0 & A_{n_3 \times n_3} \end{bmatrix} B = \begin{bmatrix} B_{n_1 \times 1} & 0 & 0 \\ 0 & B_{n_2 \times 1} & 0 \\ 0 & 0 & B_{n_3 \times n_1} \end{bmatrix} \quad (13)$$

$$C = \begin{bmatrix} 0 & C_{1 \times n_2} & 0 \\ C_{1 \times n_1} & 0 & C_{1 \times n_3} \end{bmatrix} D = \begin{bmatrix} 0 & D_{1 \times 1} & 0 \\ D_{1 \times 1} & 0 & D_{1 \times 1} \end{bmatrix}, \quad (14)$$

where  $n_1$ ,  $n_2$  and  $n_3$  are here orders of controllers  $K_1$ ,  $R_2$  and  $F$  respectively.

### 5.2. Weighting filters selection

The bandwidth of the reference angular rate that is to be tracked should certainly be below the gyro's bandwidth  $f_{bw}$ . Adding the requirement of precise tracking at low frequencies with the error as low as  $-60$  dB specifies the filter  $W_1$  completely:

$$W_1 = \frac{0.2s + 50}{s + 0.05}.$$

The filter  $W_2$  is selected such that effect of the disturbance  $\omega_c$  on the misalignment  $e_\varphi$  is minimized and kept below  $0.09$  rad, which is the mechanical limit of angle  $e_\varphi$  over all frequencies. Moreover the low frequency disturbances and especially the steady state disturbance should be attenuated by more than  $-60$  dB. These requirements are fulfilled by the filter

$$W_2 = \frac{10s + 100}{s + 0.025}.$$

To improve the attenuation of the effect of disturbance  $\omega_c$  in the inertial velocity loop up to frequency  $1$  Hz, where the unwanted oscillation of the carrier is expected, an additional filter

$$W_c = \frac{2s + 3.6}{s + 3.6}$$

is placed at the  $\omega_c$ 's input.

Since both the input voltages are normalized (to unity) the simple choice of filter penalizing the actuator effort is  $W_{u1} = W_{u2} = 1$ .



### 5.3. Resulting controller

Since HIFOO relies on the algorithm that searches only for local minima, to initiate the HIFOO optimization routine, one needs to specify not only the augmented plant  $P$ , the required structure of the controller state space matrices  $A$ ,  $B$ ,  $C$ ,  $D$  (in our situation with structure (13) and (14) with the orders  $n_1 = 1$ ,  $n_2 = 2$  and  $n_3 = 2$ ), but also an "initial controller". The task of searching for the structured  $H_\infty$  optimal controller may be then interpreted as refining already known controllers  $K_1$  and  $R_2$ . These two are empirically tuned PI controllers  $K_1 = (s + 100)/s$  and  $R_2 = 10(s + 0.5)/s$  and were used to build the initial compound controller  $K$ . The state space realization of the resulting controller is

$$A = \begin{bmatrix} -1.3 & 0 & 0 & 0 & 0 \\ 0 & -14.1 & 1.6 & 0 & 0 \\ 0 & -0.5 & -1.3 & 0 & 0 \\ 0 & 0 & 0 & -12.2 & -86.6 \\ 0 & 0 & 0 & -12.5 & -89.1 \end{bmatrix} \quad B = \begin{bmatrix} -0.48 & 0 & 0 \\ 0 & 5.48 & 0 \\ 0 & -2.03 & 0 \\ 0 & 0 & 5.20 \\ 0 & 0 & -2.37 \end{bmatrix} \quad (15)$$

$$C = \begin{bmatrix} 0 & 10.11 & 1.39 & 0 & 0 \\ -0.57 & 0 & 0 & 4.98 & 9.86 \end{bmatrix} \quad D = \begin{bmatrix} 0 & 1.26 & 0 \\ 0.33 & 0 & 17 \end{bmatrix}. \quad (16)$$

Observe the structure in the matrices. Bode plots of the resulting HIFOO controller together with the plots of classically tuned PI controllers designed for two decoupled subsystems are shown in Fig. 8.

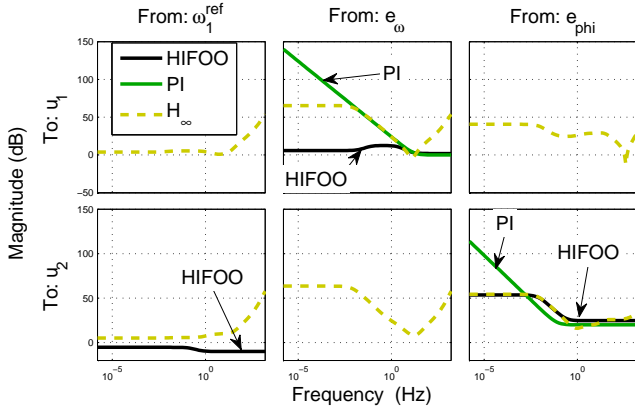


Figure 8: Magnitude Bode plots for the controller and comparison with the PI decoupled controllers. The HIFOO controller contains an extra feedforward term  $K_{(2,1)} = F$ .

### 5.4. Closed loop simulations

The designed controller given by the quadruple of matrices  $A$ ,  $B$ ,  $C$ ,  $D$  and the initial PI controllers  $K_1$  and  $R_2$  will be now used to evaluate the closed-loop transfer functions. Fig. 9 shows the closed-loop transfer functions from the exogenous inputs (disturbance and reference) to the regulated (error) signals. The requirements on reference tracking were successfully accomplished with 10 Hz bandwidth. The disturbance transfer to the inner stage (from  $\omega_c$  to  $\omega_1$ ) were rejected to  $-20$  dB in the worse case. The misalignment angle  $e_\varphi$  is very well regulated too since the worst case value of  $-30$  dB suffices to avoid reaching the  $\pm 5^\circ$  mechanical limit (supposing the amplitude of disturbance is bounded by 1 rad/s).

Fig. 10 then follows with the closed-loop transfer functions from the disturbance and the reference signal to the control signals (actuator outputs). All of these frequency responses are below the 0 dB value except for the top left figure. This means that the controller signal saturation may occur in case of the PI controller. This will happen only for reference signals changing faster than  $\approx 0.5$  rad/s since the overshoot is less than 6 dB.

Finally, Fig. 11 complements frequency response plots with the responses to step changes in reference and disturbance inputs.

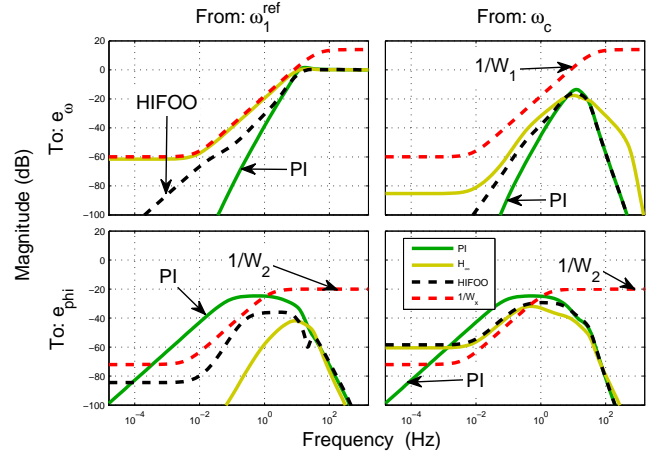


Figure 9: Magnitude Bode plots for the closed-loop transfer functions (from the disturbances and references to the error signals).

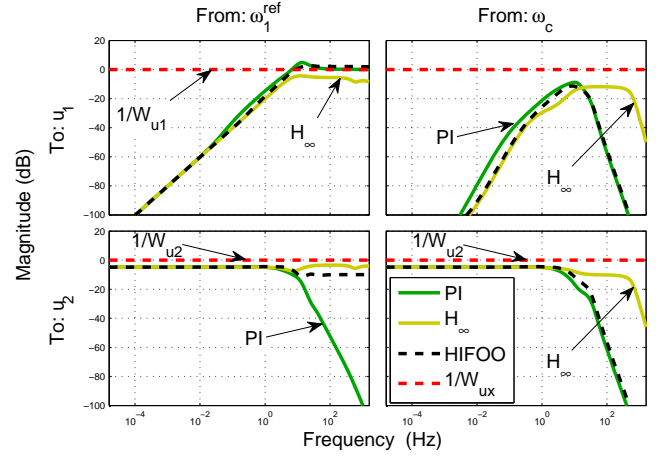


Figure 10: Magnitude Bode plots for the closed-loop transfer functions.

## 6. Experimental verification

The experimental dual-stage benchmark system allows verification of the designed controllers directly from Matlab (by The Mathworks) using Real-Time Toolbox via general-purpose

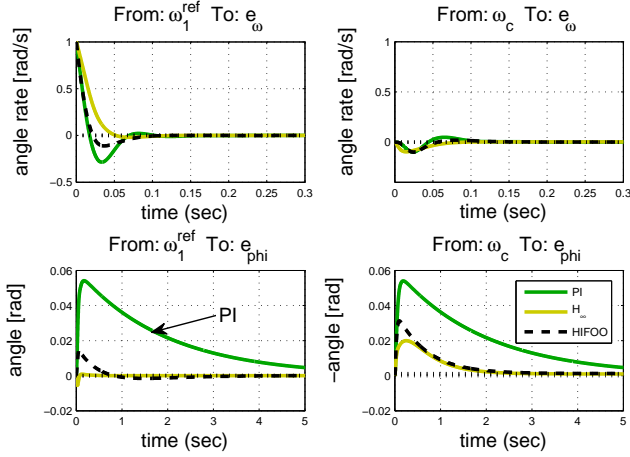


Figure 11: Closed-loop step responses. The response of angle  $e_\varphi$  is improved comparing to initial PI controller. Comparing bottom graphs shows the usefulness of the feedforward term  $F$  – the reference signal  $\omega_1^{ref}$  viewed as a disturbance is better rejected by outer joint in case of HIFOO. Note the minus mark at y-label.

DAQ card MFC624, both produced by Humusoft. The sampling rate of the algorithm was set up to 1 kHz. Two experiments were conducted with the HIFOO controller (15) – (16).

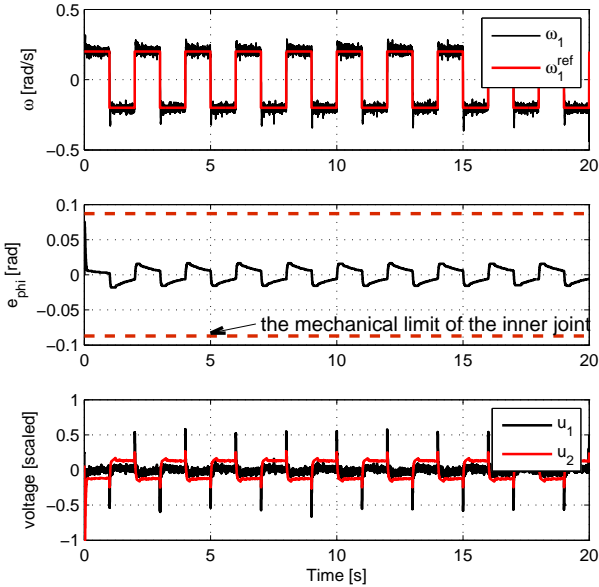


Figure 12: The experimental results of reference  $\omega_1^{ref}$  tracking.

In Fig. 12 and Fig. 13, the reference tracking was demonstrated. During the fast raising edge of the steps, the angle  $e_\varphi$  is increased at first and then slowly reaching zero, but always remains inside  $\pm 5^\circ$  region as desired.

In Fig. 14, a satisfactory disturbance rejection is shown. System was exposed to disturbing rotational motion of the base, with the (recorded) angular rate  $\omega_c$  of amplitude up to 2 rad/s. The inner stage (driven by the voice coil motor) has sufficiently

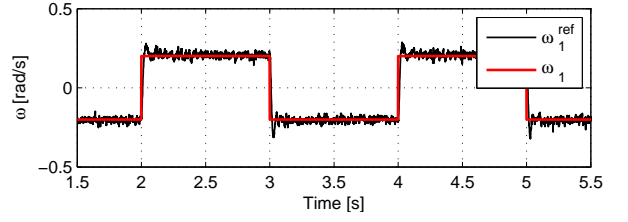


Figure 13: Detail of the  $\omega_1^{ref}$  reference tracking from Fig. 12.

attenuated the influence of this disturbance as the graph of  $\omega_1$  shows. An exceptional short moment is at time 6.6 s when the angle  $e_\varphi$  reached its mechanical limit.

## 7. Conclusion

The paper described a practical application of a freely available HIFOO toolbox for a low-order  $\mathcal{H}_\infty$ -(sub)optimal controller design with a specified structure.

In particular, a single-axis electromechanical motion control system with two motorized stages — so-called dual stage system — was introduced and described in a great technical detail. Such benchmark system is motivated by inertial stabilization systems for optoelectronic payloads carried by mobile carriers.

The system offers two variables for measurement and two independent actuators, hence, the problem can be tackled either by using classical techniques based on cascading SISO loops, or direct design of a MIMO controller. Combining benefits of both approaches, a structured MIMO approach is chosen. The structure was dictated by the use of two decoupled controllers complemented by a feedforward term.

Both numerical simulations and laboratory experiments support the conclusion that the degradation of the closed-loop performance was negligible compared to the full  $\mathcal{H}_\infty$ -(sub)optimal controller. The simplified implementation and tuning presents a major benefit.

## 8. Acknowledgements

The authors thank the authors of HIFOO for turning their high-quality scientific work into a practically usable software tool.

## References

- Canudas de Wit, C., Olsson, H., Åström, K. J., Lischinsky, P., 1995. A new model for control of systems with friction. *IEEE Transactions on Automatic Control* 40 (3), 419–425.
- Gumussoy, S., Henrion, D., Millstone, M., Overton, M., 2009. Multiobjective robust control with HIFOO 2.0. In: *Proceedings of the IFAC Symp. on Robust Control Design*.
- Herrmann, G., Guo, G., Mar. 2004. HDD dual-stage servo-controller design using a  $\mu$ -analysis tool. *Control Engineering Practice* 12 (3), 241–251.
- Hilkert, J. M., Feb. 2008. Inertially stabilized platform technology: concepts and principles. *Control Systems Magazine, IEEE* 28, 26–46.
- Horowitz, R., Li, Y., Oldham, K., Kon, S., Huang, X., 2007. Dual-stage servo systems and vibration compensation in computer hard disk drives. *Control Engineering Practice* 15 (3), 291–305.

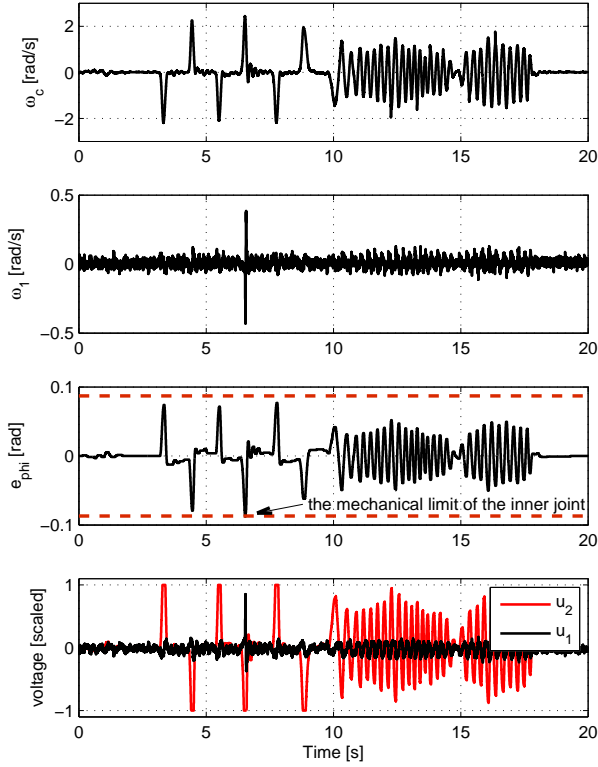


Figure 14: The experimental result of  $\omega_c$  rejection. At time 6.6 s the misalignment angle  $e_\varphi$  has reached its mechanical limit and the disturbance passed into  $\omega_1$  as well. In cases where  $\omega_c$  was higher than the scaled 1 rad/s, the saturation of  $u_2$  was observed.

- Hurák, Z., Řezáč, M., December 2009. Combined line-of-sight inertial stabilization and visual tracking: application to an airborne camera platform. In: Proc. of 48th IEEE Conference on Decision and Control. Shanghai, China.
- Hurák, Z., Řezáč, M., In Press. Image-based pointing and tracking for inertially stabilized airborne camera platform. IEEE Transactions on Control Systems Technology.
- Lyou, J., Kang, M., Kwak, H., Choi, Y., 2009. Dual stage and an image processing-based method for sight stabilization. Journal of Mechanical Science and Technology 23 (8), 2097–2106.
- Masten, M., Feb. 2008. Inertially stabilized platforms for optical imaging systems: tracking dynamic targets with mobile sensors. IEEE Control Systems Magazine 28, 47–64.
- Åström, K. J., Hägglund, T., Aug. 2005. Advanced PID Control. The Instrumentation, Systems, and Automation Society.
- Ray, L., Ramasubramanian, A., Townsend, J., 2001. Adaptive friction compensation using extended kalman-bucy filter friction estimation. Control Engineering Practice 9 (2), 169–179.
- Schroek, S., Messner, W., McNab, R., 2001. On compensator design for linear time-invariant dual-input single-output systems. IEEE/ASME Transactions on Mechatronics 6 (1).
- Suthasun, T., Mareels, I., Al-Mamun, A., 2004. System identification and controller design for dual actuated hard disk drive. Control engineering practice 12 (6), 665–676.
- Woody, S., Smith, S., 2006. Design and performance of a dual drive system for tip-tilt angular control of a 300 mm diameter mirror. Mechatronics 16 (7), 389–397.
- Zheng, J., Salton, A., Fu, M., 2011. Design and control of a rotary dual-stage actuator positioning system. Mechatronics.